

DOI: 10.1002/

Article type: Full Paper

Full energy spectra of interface state densities for *n*- and *p*-type MoS₂ field-effect transistors

Nan Fang⁺, Satoshi Toyoda, Takashi Taniguchi, Kenji Watanabe, and Kosuke Nagashio*

Dr. N. Fang, S. Toyoda, Prof. K. Nagashio

Department of Materials Engineering, The University of Tokyo 113-8656, Japan

⁺Present address: RIKEN, Wako, Saitama 351-0198, Japan

E-mail: nagashio@material.t.u-tokyo.ac.jp

Dr. T. Taniguchi, Dr. K. Watanabe

National Institute of Materials Science, Ibaraki 305-0044, Japan

Keywords: two-dimensional material, heterostructure, defect states, quantum capacitance

Abstract:

Two-dimensional (2D) layered materials are promising for replacing Si to overcome the scaling limit of recent ~5 nm-length metal-oxide-semiconductor field-effect transistors (MOSFETs). However, the insulator/2D channel interface severely degrades the performance of 2D-based MOSFETs, and the origin of the degradation remains largely unexplored. Here, we present the full energy spectra of the interface state densities (D_{it}) for both *n*- and *p*- MoS₂ FETs, based on the comprehensive and systematic studies, *i.e.*, thickness range from monolayer to bulk and various gate stack structures including 2D heterostructure with *h*-BN as well as typical high-*k* top-gate structure. For *n*-MoS₂, D_{it} around the mid gap is drastically reduced to $5 \times 10^{11} \text{ cm}^{-2} \text{ eV}^{-1}$ for the heterostructure FET with *h*-BN from $5 \times 10^{12} \text{ cm}^{-2} \text{ eV}^{-1}$ for the high-*k* top-gate MoS₂ FET. On the other hand, D_{it} remains high, $\sim 10^{13} \text{ cm}^{-2} \text{ eV}^{-1}$, even for the heterostructure FET for *p*-MoS₂. The systematic study elucidates that the strain induced externally through the substrate surface roughness and high-*k* deposition process is the origin for the interface degradation on the conduction band side, while sulfur-vacancy-induced defect-states dominate the interface degradation on the valance band side. The present understanding on the interface properties provides the key to further improving the performance of 2D FETs.

1. Introduction

The electric field effect that enables modulation of the carrier density in a semiconductor channel is at the heart of the transistor. The gate controllability represented by the subthreshold swing (*S.S.*), that is, gate-voltage change needed to induce a drain-current change of one order of magnitude, is critical to achieve energy-efficient logic devices.^[1] Therefore, for Si metal-oxide-semiconductor field-effect transistors (MOSFETs), many dedicated researchers have developed interface

analysis methods based on capacitance-voltage (*C-V*) measurements and have studied the SiO₂/Si interface properties in great detail such that they have become reliable and widely accepted.^[2-11] Here, the recent demonstration of a natural thin-body MoS₂ FET with an effective channel length of ~3.9 nm has facilitated research on 2-dimensional (2D) layered channels due to overcoming the scaling limit of ~5 nm for Si gate length.^[12] Although the dangling-bond-free surface of the layered channel is expected to ideally provide an electrically inert interface, there are many reports on the wide range of interface state densities (D_{it})

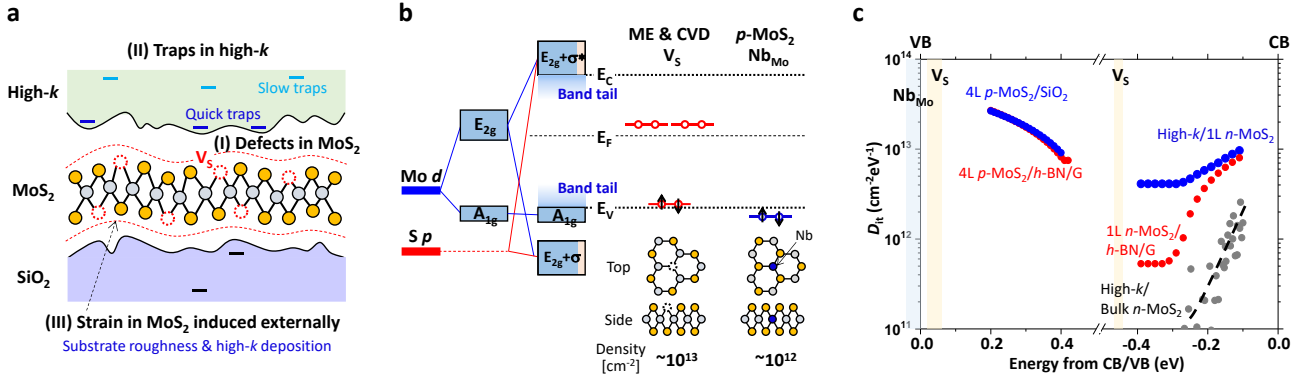


Figure 1. (a) Schematic illustration of different origins of interface states in high-*k*/MoS₂/oxide structures. (b) Schematic bonding diagram showing how the local orbitals on Mo and S interact to form CB, VB, and interface states in MoS₂. V_S and Nb_{Mo} indicate the sulfur vacancy and the substitution of Mo site by Nb, respectively. (c) The full energy spectra of D_{it} for different gate stack structures. Notice that the band gaps of 1L, 4L, and bulk MoS₂ are different. Therefore, the transverse axis for the D_{it} - energy distribution is shown as the energy from the CB/VB edge. For the high-*k*/bulk *n*-MoS₂ interface, D_{it} is extracted from frequency dispersion-free *C-V* curves by the Terman method.^[25] The bulk MoS₂ thickness is ~ 58 nm, which is larger than W_{Dm} , supporting the availability of the *C-V* measurement. $N_D = 2 \times 10^{17}$ cm⁻³ is used here for a natural *n*-MoS₂ crystal, which is precisely determined from thickness-dependent *I-V*, *C-V* characterizations.

from $10^{11} \sim 10^{13}$ eV⁻¹cm⁻² for high-*k* top-gate *n*-MoS₂ FET in reality,^[13-30] which must be reduced to improve the device performance. To date, several physical origins for D_{it} have been proposed, which are summarized in **Figure 1a**.

First, trap (I) represents the defects and impurities in the *n*-MoS₂ channel. Sulfur vacancies (V_S) with the high density of $\sim 10^{13}$ cm⁻² are widely recognized in mechanically exfoliated (ME) and chemically vapor deposited (CVD) MoS₂.^[31-37] Since physical vapor deposited MoS₂ dominantly includes antisite defects,^[31] the present study only focus on V_S in ME and CVD MoS₂. V_S introduces defect states in the band gap, as shown in **Figure 1b**, which has been evaluated by density functional theory (DFT). CB and VB refer to the conduction band and valence band, respectively. Second, trap (II) represents the traps in the high-*k* insulator. In general, the back SiO₂ oxide is formed by thermal oxidation with well-controlled quality, which usually shows an extremely low trap site density inside ($\sim 10^{10}$ cm⁻²). On the other hand, the top high-*k* oxide is typically formed on the inert MoS₂ surface by atomic layer deposition (ALD) at a relatively low temperature with the aid of a buffer layer, which may introduce many traps inside. The traps close to the interface serve as quick traps while the traps inside the

oxide serve as slow traps, as discussed in several reports.^[24,28,38] Third, trap (III) represents the strain in MoS₂ induced externally. One of the interesting properties of 2D materials is that they can be scaled down to atomic thickness. Strain is easily induced in a thin MoS₂ channel by both substrate surface roughness and/or the high-*k* deposition process, resulting in Mo-S bond bending.^[25-27,39] Since the conduction and valence bands of MoS₂ are mainly composed of the energy splitting of the Mo *d* orbital,^[40,41] the band tail states will be easily introduced, as schematically illustrated in **Figure 1b**. Although V_S introduces lattice disorder strain around V_S in the ideally flat MoS₂ layer, this strain has already been incorporated in the DFT calculation and is regarded as the origin in trap (I). The macroscopic strain introduced externally in the MoS₂ layer is considered here in trap (III).

The high-*k*/MoS₂ interface properties are inherently complex because D_{it} includes one or more types of traps and some origins might be related to each other. Most of the previous studies only focus on one specific gate stack with limited channel thickness (t_{ch}) for *n*-type MoS₂. Therefore, a common understanding of the origin for the interface states has not yet been obtained. Although the energy distribution of D_{it} is critical to

reveal its origin from the comparison with the DFT calculation, a recent study indicated that the conventional C - V method for the D_{it} - energy relation developed for Si systems cannot be simply applied to the FET structure of 2D channels because the channel charging process due to the high channel resistance is more dominant than the electron capture/emission process by the interface trap.^[25] In this study, in order to obtain the energy distribution of D_{it} , we performed the modeling of I_D - V_{TG} characteristics^[25,26] by considering the MoS₂ channel carrier statistics through the quantum capacitance (C_Q) and its transport through the Drude model.^[42] Based on the systematic investigation of over 100 devices for both n - and p - MoS₂ with a wide thickness range of 1 layer (L) to bulk and various gate stack structures including a 2D heterostructure with h -BN as well as typical high- k top gate structure, the whole picture of high- k /MoS₂

interface is discussed.

2. Results and Discussion

2.1. Interface States of MoS₂ on the Conduction Band Side

A natural n -type MoS₂ crystal was first studied, whose thin flakes were prepared by mechanical exfoliation. **Figure 2a** shows a schematic drawing of (i) the top-gate MoS₂ FET on insulating quartz or SiO₂/Si substrates. The quartz substrate with a surface roughness similar to SiO₂ was used because the parasitic capacitance can be neglected. The typical drain/source current (I_{DS}) – top-gate voltage (V_{TG}) characteristics for 1L MoS₂ can be found in **Figure 2c**. The two-terminal field-effect mobility (μ_{FE}) are extracted to be 6.2 cm² V⁻¹ s⁻¹ under the conditions where the contribution of C_Q is neglected and C_{ox} for the Y₂O₃ buffer layer (1 nm) and the ALD-Al₂O₃ (10 nm) is estimated as $\sim 0.45 \mu\text{Fcm}^{-2}$ at the

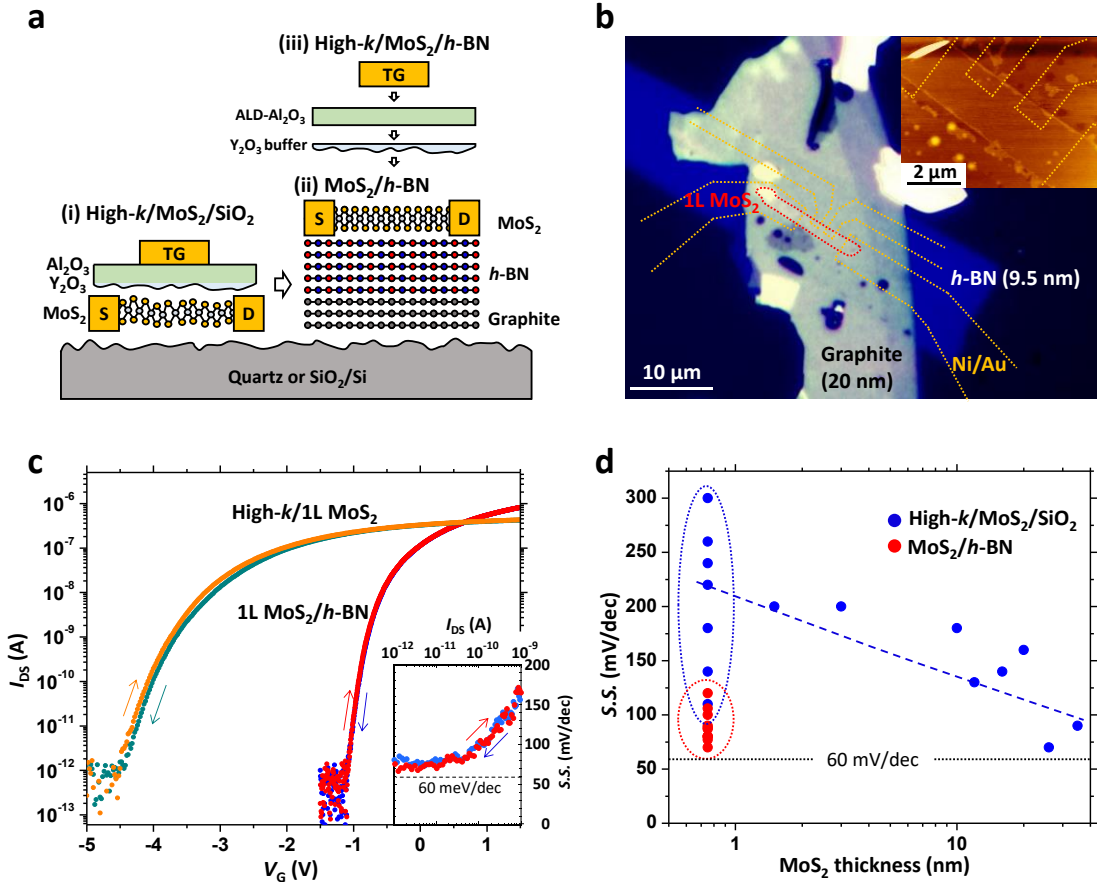


Figure 2. (a) Schematics of (i) high- k /MoS₂/SiO₂, (ii) MoS₂/ h -BN, (iii) high- k /MoS₂/ h -BN FETs. (b) The optical image of a back-gate MoS₂/ h -BN FET. Inset shows the AFM image. (c) I_{DS} - V_G characteristics of high- k /1L MoS₂ (top-gate sweep), 1L MoS₂/ h -BN FETs (back-gate sweep) at $V_{DS} = 0.1$ V and RT. Inset shows $S.S.$ as a function of I_{DS} for 1L MoS₂/ h -BN FET. (d) $S.S.$ as a function of MoS₂ thickness for high- k /MoS₂/SiO₂ and MoS₂/ h -BN FETs.

accumulation in C - V . The hysteresis is relatively small. $S.S.$ extracted at the current range of $\sim 10^{-12}$ - 10^{-10} A is mainly discussed in this paper and can be expressed as^[1,25]

$$S.S. = \ln 10 \frac{k_B T}{e} \frac{C_{ox} + C_{it}}{C_{ox}}, \quad (1)$$

where k_B , T , and e are defined as the Boltzmann constant, temperature, and elementary charge, respectively. C_{ox} is the oxide capacitance, and C_{it} is the interface states capacitance ($C_{it} = e^2 D_{it}$). $S.S.$ is a simple and effective parameter to directly evaluate D_{it} from 1L to bulk MoS₂ with $t_{ch} \ll$ maximum depletion width ($W_{Dm} = \sim 48$ - 55 nm).^[25] C_Q or depletion capacitance (C_D) decreases exponentially with the energy. At the deep subthreshold region, $C_Q(C_D) \ll C_{it}$, which make them negligible. This relation can be clearly seen in **Figure S4b** (Supporting Information).

Figure 2d summarizes $S.S.$ as a function of t_{ch} for a top-gate MoS₂ FET on the quartz substrate. 1L MoS₂ typically has a high $S.S.$ level (~ 230 mV/dec) with a large variation. D_{it} is estimated to be $\sim 8 \times 10^{12}$ cm⁻²eV⁻¹. By increasing t_{ch} over 20 nm, $S.S.$ can be reduced as low as ~ 80 mV/dec with small variation, which corresponds to a D_{it} of $\sim 9 \times 10^{11}$ cm⁻²eV⁻¹. The top-gate fabrication process is the same in principle from 1L to

in MoS₂, and/or trap (III), the strain in MoS₂ induced externally, are the main origins for the high D_{it} of atomically thin MoS₂. In particular, as for trap (III), it mainly comes from the Mo-S bond bending. Therefore, the thick bulk MoS₂ is robust to this effect, which accounts for the smaller $S.S.$ with increasing the MoS₂ thickness.

To clarify the importance of trap (III) and achieve low D_{it} even for the 1L MoS₂ channel toward the ultimately scaled device applications, the MoS₂/ h -BN/graphite heterostructure FET was prepared as shown schematically by (ii) in **Figure 2a**. The optical image is also shown in **Figure 2b**. The details of the transfer process with negligible bubbles is explained in **Figure S1** (Supporting Information).^[43,44] The utilization of back-gate graphite can help with increasing C_{ox} (0.23 μ Fcm⁻² with dielectric constant of 2.5 for h -BN) comparable to that for the high- k top gate by reducing the h -BN thickness to 9.5 nm, since the atomically flat surface of h -BN is guaranteed by the total thickness of graphite and h -BN (> 20 nm) (**Figure S1**, Supporting Information). Thus, $S.S.$ for the 2D heterostructure FET can be compared with those for the high- k /MoS₂ FETs. Moreover, no high- k deposition is conducted on the MoS₂ channel to avoid any strain, which

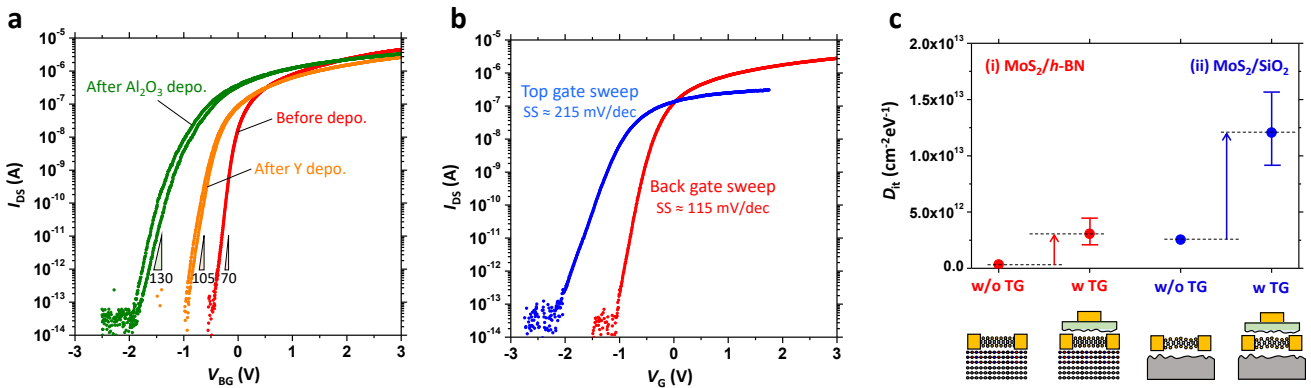


Figure 3. (a) I_{DS} - V_{BG} characteristics of 1L MoS₂/ h -BN FET at $V_{DS} = 0.1$ V and RT before top-gate deposition, after Y₂O₃ buffer layer deposition, and after ALD-Al₂O₃ deposition. (b) I_{DS} - V_G characteristics of dual-gate high- k /1L MoS₂/ h -BN FET. (c) The increase in D_{it} by the top-gate deposition process for back-gate 1L MoS₂/SiO₂ FETs and 1L MoS₂/ h -BN FETs, respectively.

bulk, which means that trap (II), traps in the oxide, is unlikely the dominant origin for D_{it} - t_{ch} dependence. Instead, trap (I), the defects

indicates that two origins for trap (III), that is, substrate surface roughness and high- k deposition, have been suppressed in the

present 2D heterostructure FETs. The corresponding I_{DS} – back-gate voltage (V_{BG}) characteristics at room temperature (RT) in **Figure 2c** clearly show the improvement of $S.S.$ (~ 75 mV/dec) with negligible hysteresis $\Delta V_{hys} = 7.3$ mV, where the corresponding D_{it} is $\sim 4 \times 10^{11}$ cm⁻²eV⁻¹. The μ_{FE} values for two probe (2P) and four probe (4P) measurements are comparable (~ 70 cm²V⁻¹s⁻¹) due to an ohmic contact by Ni (**Figure S2**, Supporting Information). More than ten 2D heterostructure FET devices were fabricated and show smaller variation compared with high- k top-gate FET devices, as shown in **Figure 2d**. Since 1L MoS₂ flakes are mechanically exfoliated from the same natural MoS₂ crystals for both high- k top gate and 2D heterostructure FETs, trap (I) is unlikely the main origin for the considerably low D_{it} . Instead, the low D_{it} is most likely from the suppression of trap (III), which is achieved by forming the atomically flat surface and avoiding the high- k deposition process.

A nearly ideal MoS₂/ h -BN interface is obtained by the 2D heterostructure formation. Here, it is interesting to reveal how the interface is degraded during the high- k deposition. Therefore, a 1-nm thick Y₂O₃ buffer layer, 30 nm-thick ALD-Al₂O₃ and Al top-gate metal were sequentially deposited on a newly prepared 1L MoS₂ heterostructure FET device, as schematically shown by (iii) in **Figure 2a**. The degradation of $S.S.$ by the top-gate deposition was monitored through the back interface by the back-gate sweep, as shown in **Figure 3a**. In this device, C_{ox} of h -BN with the thickness of 8.1 nm is 0.27 μ Fcm⁻² and the thickness of graphite is 29 nm. $S.S. = \sim 70$ mVdec⁻¹ before the top-gate deposition increases to ~ 105 mVdec⁻¹ after the Y buffer layer deposition and finally to ~ 130 mVdec⁻¹ after the subsequent ALD-Al₂O₃ process. The corresponding D_{it} values are $\sim 3.4 \times 10^{11}$ cm⁻²eV⁻¹, $\sim 1.3 \times 10^{12}$ cm⁻²eV⁻¹, and $\sim 1.9 \times 10^{12}$ cm⁻²eV⁻¹, respectively. The hysteresis also increases to 0.14 V. However, when $S.S.$ was measured again before the Al top-gate deposition, $S.S.$ unintentionally improved to ~ 90 mVdec⁻¹, as shown in **Figure S3**

(Supporting Information). This result strongly indicates that the degradation of both D_{it} and hysteresis originates mainly from the strain induced by the high- k deposition process, not from the defect formation (V_s) in MoS₂ during the deposition. It should be emphasized that the Y buffer layer is deposited under the Ar pressure of 10⁻¹ Pa to entirely suppress the deposition damage in this study.^[45,46]

In the case of Si on an insulator (SOI), the top and back interfaces are still separated even for a 7-nm thick Si channel.^[47] On the other hand, for a 1L MoS₂, high- k top-gate deposition considerably affects the back interface. To analyze the top and back interface quantitatively, the top-gate I_{DS} - V_{TG} characteristics was measured, as shown in **Figure 3c**. Although the back-gate $S.S.$ (115 mVdec⁻¹) is better than top gate $S.S.$ (215 mVdec⁻¹), this result is not fair comparison because C_{ox} for the top and the back are different. Therefore, C_{ox} for a top-gate insulator is extracted to be 0.16 μ Fcm⁻² from the top-gate and back-gate capacitive coupling method; then, D_{it} is estimated. It is interesting that the back-interface D_{it} (1.9×10^{12} cm⁻²eV⁻¹) is almost the same as the top-interface D_{it} (2.6×10^{12} cm⁻²eV⁻¹), which reveals that both top and bottom interfaces must be controlled properly because both interfaces interact with each other for atomically thin 2D channels.

To further separate the contribution of the strain induced by the substrate surface roughness and high- k deposition process in trap (III), the degree of the interface degradation by the high- k deposition is compared for back-gate 1L MoS₂/SiO₂/Si and 1L MoS₂/ h -BN/graphite heterostructure FETs. D_{it} is extracted before and after the high- k deposition. As shown in **Figure 3c**, D_{it} increases for both substrates after the high- k deposition but more drastically degrades for MoS₂ on the rough substrate surface, that is, SiO₂/Si. The most important finding here is that the degradation of $S.S.$ is drastically enhanced in response to the degree of initial substrate surface roughness. Therefore, the strategy to obtain the sharp switching of an atomically thin 2D channel

toward the ultimately scaled device applications is to develop stress-free high- k deposition while maintaining the atomic flatness of the substrate surface.

2.2. Energy Spectra of Interface States of n -MoS₂

The interfacial properties discussed above are based on $S.S.$ at the deep subthreshold region, which does not provide a precise energy level for D_{it} in the energy band gap. Here, D_{it} is extracted as a function of energy from I - V characteristics^[25,26] by considering the carrier statistics through C_Q and its transport through the Drude model.^[42] An example of this simulation is shown in **Figure S4** (Supporting Information). When the ideal I_{DS} - V_{TG} curve is calculated using C_{ox} and C_Q with a constant μ value extracted experimentally, the ideal $S.S.$ of 60 mV/dec can be obtained. The deviation between the ideal and experimental I_{DS} - V_{TG} can be considered as the contribution of electron traps to the interface states, that is, C_{it} . By assuming the energy distribution of C_{it} as a fitting parameter, the energy distribution of D_{it} of n -MoS₂ is estimated for high- k /1L-MoS₂/SiO₂ device with top-gate sweep and 1L-MoS₂/ h -BN device with back-gate sweep. On the other hand, for high- k /bulk MoS₂/SiO₂, D_{it} is extracted as a function of energy from C - V characteristics by the Terman method.^[25] The D_{it} -energy distribution is shown in **Figure 1c**. The present analysis can quantitatively capture the band-tail shaped D_{it} , which cannot be obtained by the simple D_{it} estimation from $S.S.$. Interestingly, the existence of mid-gap states is evident for high- k /1L-MoS₂/SiO₂ and 1L-MoS₂/ h -BN cases because a constant $S.S.$ region exists below the current level of $\sim 10^{-11}$ A, as shown in the inset of **Figure 2c**. Although the mid-gap states are close to the energy for V_S , the mid-gap states and band tail states are simultaneously reduced by improving the flatness of the substrate. To further emphasize the substrate flatness instead of V_S effect, **Figure S5** (Supporting Information) shows that D_{it} -energy distribution for high- k /1L-MoS₂/ h -BN both from top-gate sweep is smaller than that for

high- k /1L-MoS₂/SiO₂ in the whole measured energy range. It is evident that trap (I) is not the main origin for D_{it} in our devices, even though V_S induced defect-states have been widely discussed as the origin for the degradation of the electrical properties for MoS₂. As discussed in the previous section, the strain induced by high- k deposition is the dominant origin of the degradation. The interesting point here is that D_{it} near the CB edge for 1L-MoS₂/ h -BN is similar to that for high- k /1L-MoS₂/SiO₂ despite the lack of high- k deposition, which is much larger than that for high- k /bulk MoS₂. This finding suggests that there is still much room for improvement. At present, the way to improve is not clear yet; the origin may not be the same since the CB minimum changes from the K point for a monolayer to the point on the K \rightarrow Γ line for the bulk material.^[48,49]

2.3. Electron Transport of n -MoS₂

Having clarified the interfacial properties, the transport properties related to the interface states were studied through the temperature dependence for the high- k /MoS₂/ h -BN devices. **Figure 4a** shows the temperature dependence of I_{DS} - V_{BG} characteristics before the top-gate deposition. The threshold voltage is shifted positively by lowering the temperatures. This is due to the temperature dependence of C_Q of 1L MoS₂, as shown in **Figure S4** (Supporting Information), which is further amplified by D_{it} . $S.S.$ also decreases by lowering the temperature at the range of 150-300 K. This is understood using Equation 1, which is the common case for a bulk Si MOSFET. However, $S.S.$ values remain almost constant at 50 -150 K and start to increase at the temperature below 50 K. This result suggests the transition of the electron transport mechanism, that is, the occurrence of interface-states-related transport, such as nearest neighbor hopping (NNH) and variable range hopping (VRH),^[34,50,51] because Equation 1 is based on carrier drift/diffusion through the band transport. **Figure 4b** shows I_{DS} - V_{BG} characteristics after the top-gate deposition. The threshold voltage shifts positively more substantially

by lowering the temperatures, which is due to the increased D_{it} . S.S. is still proportional to the temperature at the higher temperature region, as shown in **Figure 4c**. In contrast, at the lower temperature region in **Figure 4b**, conductance fluctuation becomes apparent with high repeatability, which further degrades the S.S. Since the metal/MoS₂ contact is not affected by the top-gate deposition, it cannot be the origin of the observed conductance fluctuation. The conductance fluctuation does not show resonant tunneling behavior.^[52] Therefore, this is most likely from the interference of carrier hopping path by localized states.

To further clarify the above scenario quantitatively, **Figure 4d** shows the temperature dependence of I_{DS} at different

device. So far, the temperature dependence of I_{DS} for the MoS₂ FET is explained by three terms, which are the conduction band transport by thermal activation (TA), and interface-states-related transport by NNH and VRH. Although some papers reported that VRH accounts for the observed temperature dependence of I_{DS} ,^[50,51] we found that NNH gives a reasonable fitting to experimental results at the low temperature, which can be shown by $I_{DS} = I_{TA}^0 \exp(-E_a/k_B T) + I_{NNH}^0 \exp(-E_h/k_B T)$

, where I_{TA}^0 , I_{NNH}^0 are prefactors. E_a and E_h are the band activation energy and hopping energy, respectively. E_a is the energy difference between the Fermi energy (E_F) and the CB minimum, while E_h is the energy

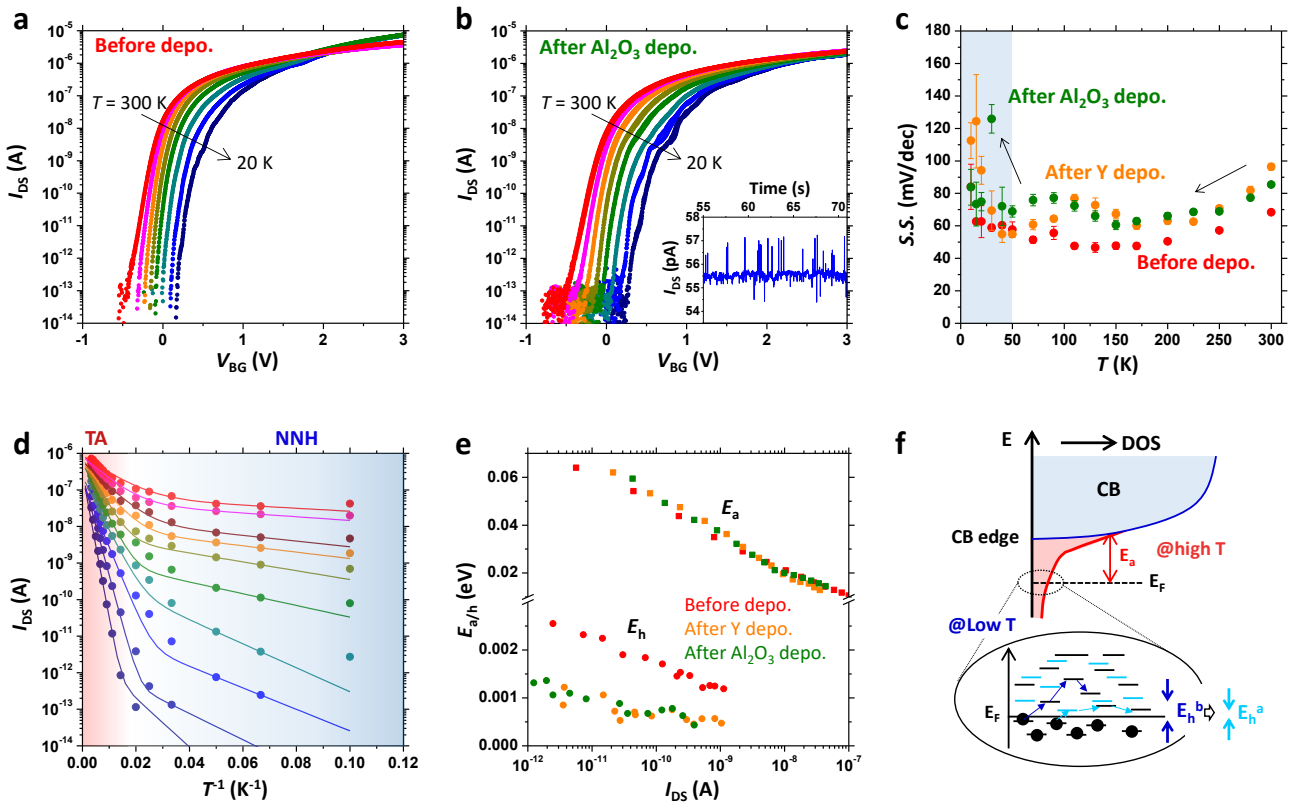


Figure 4. I_{DS} - V_{BG} characteristics of 1L MoS₂/h-BN FET at $V_{DS} = 0.1$ V and $T = 300, 250, 200, 150, 110, 70, 40,$ and 20 K (a) before Y_2O_3 buffer layer deposition and (b) after Al_2O_3 deposition. Inset shows I_{DS} as a function of time at $V_{DS} = 0.1$ V at 10 K for a different device. (c) S.S. as a function of temperature before Y_2O_3 buffer layer deposition (red), after Y buffer layer deposition (orange), after Al_2O_3 deposition (green). (d) I_{DS} as a function of T^{-1} . The solid circles indicate experimental data, while solid lines indicate the fittings. (e) E_a , E_h as a function of I_{DS} before and after the top-gate deposition. (f) Schematic illustration of the energy - DOS relation near the CB. The red hatched region just below CB edge indicates the interface states region. Magnified illustration shows the hopping transport through the interface states at low temperature. E_h^b and E_h^a indicate E_h before and after the top-gate deposition, respectively.

V_{BG} values for an $Al_2O_3/Y_2O_3/MoS_2/h-BN$ difference between the nearest unoccupied

interface states. The transition temperature of from TA to NNH (~ 50 K) is consistent with the transition temperature in the plot of the temperature dependence of $S.S.$ (**Figure 4c**). **Figure 4e** shows extracted E_a and E_h values as a function of I_{DS} through the fitting in **Figure 4d**. E_a and E_h are also included for the devices before the top-gate deposition and after the Y_2O_3 deposition. E_a remains almost unchanged before and after the top-gate deposition. This supports that the conduction band transport take place at high temperature. In contrast, E_h decreases just after Y_2O_3 deposition and no further reduction is observed after Al_2O_3 deposition. The decrease in E_h is due to the increase in D_{it} , as schematically shown in **Figure 4f**, and accounts for NNH transport at low temperatures at the subthreshold region, that is, the region of conductance fluctuation. The reduced E_h after top-gate deposition could make the hopping path sensitive to Coulombic interactions from localized states. This is then supported by the time-domain of I_{DS} from another device, which shows a similar conductance fluctuation at 10 K, as shown in the insert of **Figure 4b**. Three-level of I_{DS} are dominantly observed at the conductance fluctuation region, which shows multilevel random telegraphic signals (RTSs).^[53,54] Since the reduction of E_h for NNH accompanied with the increased D_{it} triggers the observation of RTSs, the initial deposition of insulator, that is, the buffer layer, on the 2D channel must be precisely controlled to avoid introducing strain to the 2D channel.

2.4. Interface States of MoS₂ on the Valance Band Side

Natural MoS₂ and CVD MoS₂ flakes usually show n -type behavior as discussed above. Although hole transport has been achieved using ionic gating,^[55] the substrate dielectric effect,^[56] or a contact metal design,^[57,58] these are either thermally unstable or complicated, which makes the investigation of interfacial properties difficult. Therefore, a niobium (Nb)-doped p -type MoS₂ crystal was studied here, since the substitution of Mo site by Nb (Nb_{Mo}) is thermodynamically

stable,^[59] and uniformly dispersed in MoS₂ crystal, which has been confirmed by transmission electron microscopy.^[60] **Figure 5a** compares the Raman spectra of p -MoS₂ and n -MoS₂. Both types of MoS₂ flakes show sharp E_{2g} and A_{1g} peaks and no distinct difference from 1L to the bulk material,^[61,62] which indicates that the effect of Nb substitution on the lattice phonon is negligible here.

Back-gate p -MoS₂ FETs on the SiO₂/Si substrate were then fabricated by following the same procedure as n -MoS₂, as schematically shown in **Figure 5b**. **Figure 5c** shows I_D - V_{BG} characteristics with different MoS₂ thicknesses. In contrast to n -MoS₂, p -MoS₂ FETs show strong p^+ -type behavior when $t_{ch} > \sim 8$ nm, which is consistent with previous reports,^[60] and show ambipolar behavior for 4-nm and 4L-thick devices. Interestingly, the 2L-MoS₂ device shows unipolar n -type behavior. Two-terminal hole μ_{FE} and current on-off ratio are $10.5 \text{ cm}^2\text{V}^{-1}\text{s}^{-1}$ and 10 for the 8-nm-thick p -MoS₂ and $2.5 \text{ cm}^2\text{V}^{-1}\text{s}^{-1}$ and $\sim 10^3$ for 4-nm-thick p -MoS₂, respectively. It is consistent with reported hall mobility.^[60] Hole μ_{FE} is further degraded below $1 \text{ cm}^2\text{V}^{-1}\text{s}^{-1}$ for the thinner devices. The off current is dramatically decreased by decreasing t_{ch} because the depletion layer width formed by the gate electrical field becomes close to t_{ch} .^[25] Therefore, for $t_{ch} > W_{Dm}$, off current remains high, which indicates the existence of unmodulated layers in thick p -MoS₂ and W_{Dm} can be assumed as ~ 7 nm. Bulk acceptor impurity concentration (N_A), which comes from the substitution of the Mo site by Nb, is extracted from W_{Dm} using the relation of

$$W_{Dm} = \sqrt{4\epsilon_{MoS_2} k_B T \ln(N_A/n_i)/e^2 N_A} \quad ,$$

where n_i is the intrinsic carrier density with the value of $\sim 3 \times 10^8 \text{ cm}^{-3}$ and ϵ_{MoS_2} is the dielectric constant of bulk MoS₂ in the direction normal to the basal plane, which is 6.3.^[63] The extracted N_A is $\sim 2 \times 10^{19} \text{ cm}^{-3}$, which is consistent with previous Hall measurements.^[60] In contrast, the natural n -

MoS₂ crystal has bulk donor impurity concentration (N_D) of $\sim 2 \times 10^{17} \text{ cm}^{-3}$.^[25]

There are two important phenomena observed in Nb-doped MoS₂ FETs; the p -type to n -type transition and asymmetry in electron and hole transport. The p -type to n -type transition can be understood by a surface electron accumulation effect. Recently, it was reported that V_S of $\sim 10^{13} \text{ cm}^{-2}$ is introduced “at the surface” of bulk MoS₂ flake during mechanical exfoliation, and electrons accumulate at the surface.^[64] Based on this report, the schematic to explain surface electron accumulation is shown in **Figure 5d**. For the bulk case, bulk N_A is larger than surface N_D . By decreasing t_{ch} , the p -type bulk properties cannot be preserved when the surface N_D becomes larger than bulk N_A . To support this idea, V_{BG} values at the charge neutral point (V_{CNP}) are plotted as a function of t_{ch} in **Figure 5e**. The charge neutral point (CNP) is defined as the point to change from hole to electron transport in ambipolar behavior (**Figure 5c**). Experimentally, the carrier density at CNP

($V_{\text{CNP}} \times C_{\text{ox}}$) is determined by both the surface donor N_D^S and bulk acceptor $N_A \times t_{\text{ch}}$. Here, N_D^S (cm^{-2}) is assumed as a constant to explain the accumulated electrons at the surface.^[64] Therefore, the simple relation of $V_{\text{CNP}} C_{\text{ox}} = -N_D^S + N_A t_{\text{ch}}$ can be obtained.

Figure 5e shows V_{CNP} is proportional to t_{ch} , which confirms the validity of this relation. Both N_D^S and N_A are calculated to be $8.5 \times 10^{12} \text{ cm}^{-2}$ and $2.7 \times 10^{19} \text{ cm}^{-3}$, respectively. N_A estimated here is consistent to N_A obtained from W_{Dm} . Although $N_A = 2.7 \times 10^{19} \text{ cm}^{-3}$ is a high doping concentration, it is not high enough to achieve p -type transport in 1L MoS₂ because $N_A \times 0.65 \text{ nm} = \sim 1.8 \times 10^{12} \text{ cm}^{-2}$ is much smaller than N_D^S . As a result, it is the surface doping effect that determines the carrier type at the atomically thin channel.

Another point is the asymmetry between electron and hole transport. **Figure 5e** shows the on-currents of both electrons and holes ($I_{\text{DS}}^{\text{ON}}$), which are defined as the current at $V_{\text{BG}} = +30 \text{ V}$ for electrons and at $V_{\text{BG}} = -30$

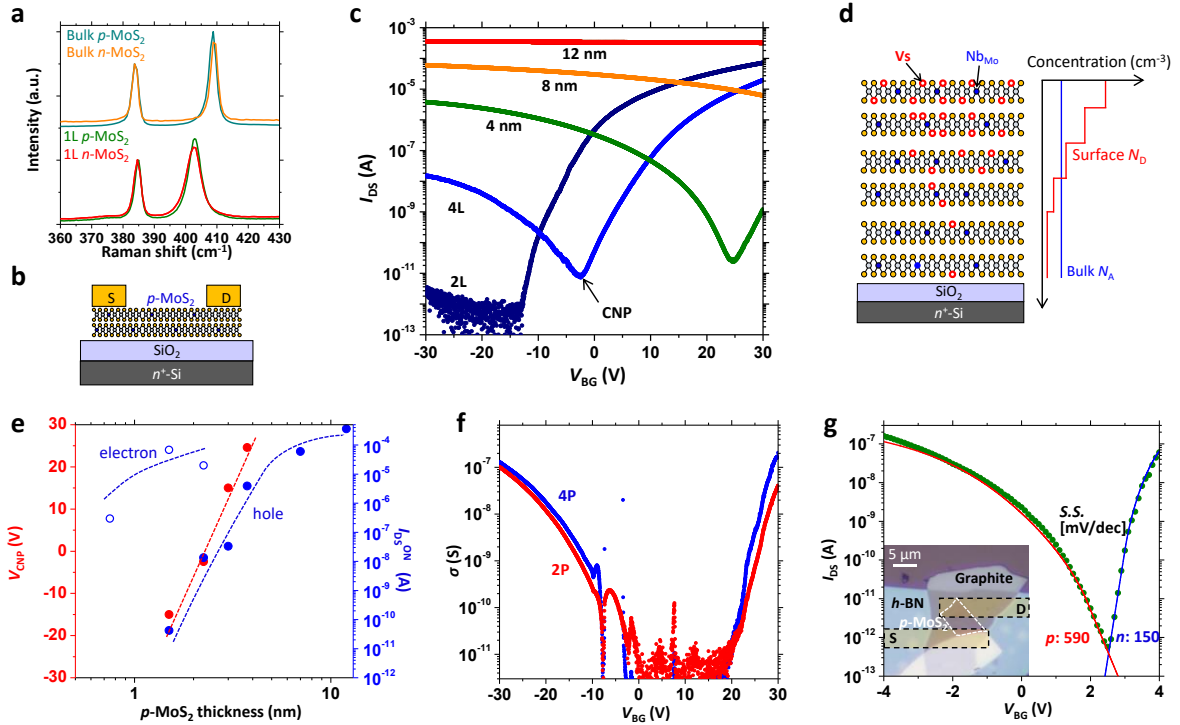


Figure 5. (a) Raman spectra of bulk, 1L n -MoS₂, and bulk, 1L p -MoS₂. (b) A schematic of a back-gate p -MoS₂/SiO₂ FET. (c) $I_{\text{DS}} - V_{\text{BG}}$ characteristics of back-gate p -MoS₂/SiO₂ FETs with different p -MoS₂ thicknesses at $V_{\text{DS}} = 1 \text{ V}$ and RT. (d) Schematic illustration of doping concentrations of bulk N_A and surface N_D as a function of thickness, showing the surface electron accumulation in p -MoS₂. (e) $I_{\text{DS}}^{\text{ON}}$ for both electrons and holes and V_{CNP} as a function of p -MoS₂ thickness. (f) $\sigma - V_{\text{BG}}$ characteristics of back-gate 4L p -MoS₂/SiO₂ FETs for both 2P and 4P measurements at 50 K. (g) $I_{\text{DS}} - V_{\text{BG}}$ characteristics (circles) and fittings (lines) at $V_{\text{DS}} = 1 \text{ V}$ and RT for a 4L p -MoS₂/h-BN/graphite heterostructure FET with the same structure shown in Figure 2a(ii).

V for holes, respectively. Although the accurate definition should be I_{DS}^{ON} at $V = |V_{BG} - V_{CNP}| = \pm 30$ V, simple definition is used here since V_{CNP} is not seen for thick p -MoS₂. The I_{DS}^{ON} of electrons is relatively stable with respect to t_{ch} , while the I_{DS}^{ON} of holes is degraded dramatically with decreasing t_{ch} even if the V_{CNP} shift is considered. For this I_{DS}^{ON} reduction, the metal/ p -MoS₂ contact effect is carefully investigated since the Schottky barrier at the contact might be the possible origin for the observed degraded hole transport. This is a quite important issue, since D_{it} cannot be simply extracted from I_{DS} - V_G if the modulation of the Schottky barrier by V_G dominantly controls the drain current.^[65,66] For n -MoS₂ with a Ni contact, we have already confirmed that the gate controls the high- k/n -MoS₂ interface, not the contact.^[25] For p -MoS₂, the contact effect is discussed as follows.

First, a 4P 4.7 nm-thick p -MoS₂ FET on a SiO₂/Si substrate with Ni contact was fabricated to quantitatively investigate the contact effect. **Figure 5f** shows conductivity (σ)- V_{BG} characteristics for both the 2P and 4P measurements at 50 K. In general, the contact property becomes dominant at low temperature, since the thermionic-emission current is drastically reduced and the field emission current becomes dominant. In **Figure 5f**, it is clear that the discrepancy between σ_{2P} and σ_{4P} is quite small. This experiment proves that the contacts for both holes and electrons are reasonably transparent because the doping concentration for both N_D and N_A is high enough. Therefore, for the degraded hole transport observed in **Figure 5c**, the metal/MoS₂ contact is not the main origin but an interfacial issue. That is, D_{it} for p -MoS₂ can be extracted similarly with n -MoS₂.

To discuss the origin of D_{it} for the VB side according to the classification in **Figure 1a**, 4L- p -MoS₂/ h -BN/graphite heterostructure FETs were fabricated for comparison, as shown in the inset of **Figure 5g**. The reason to select 4L is that it is almost the thinnest MoS₂ to show p -type conduction. Indeed, hole transport can still not be

observed for 1L p -MoS₂ heterostructure with h -BN, even though the S.S. for electrons is comparable with the n -MoS₂ heterostructure. As shown in **Figure 5g**, the S.S. for holes is ~ 590 mV/dec with $D_{it} = \sim 9.1 \times 10^{12}$ cm⁻²eV⁻¹, while it is ~ 150 mV/dec with $D_{it} = \sim 1.1 \times 10^{12}$ cm⁻²eV⁻¹ for electrons. Based on the I_{DS} - V_{BG} fitting shown by solid lines in **Figure 5g**, the energy spectra of D_{it} for the VB side are summarized in **Figure 1c**, where D_{it} for 4L- p -MoS₂/SiO₂/Si FET is also included. Interestingly, 4L p -MoS₂ for both SiO₂/Si and h -BN/graphite substrates show almost equivalent energy spectra for D_{it} with a considerably high level over 10^{13} cm⁻²eV⁻¹ regardless of the substrate flatness. This suggests that both trap (II) and trap (III) are not the main origin because of the lack of high- k deposition and the atomically flat surface of h -BN/graphite. Therefore, trap (I), that is, V_S and/or Nb_{Mo}, are the most likely the cases for p -MoS₂, because the energy levels for both V_S and Nb_{Mo} are very close to the VB maximum,^[58] as shown in **Figure 1b**.

Finally, let us discuss which defect is dominant, V_S or Nb_{Mo}. A clue can be observed in **Figure 5f** as the abnormal conductance peaks at the hole side. Very similar abnormal conductance peaks have been reported even in the hole transport for a 1L “ n -MoS₂” FET with ion gating,^[67] where it is suggested to be due to defects states by V_S close to VB. **Figure 5e** shows that the degradation of I_{DS}^{ON} for holes as a function of t_{ch} has the same tendency as the V_{CNP} shift. Since the V_{BG-CNP} shift has been suggested to be due to sulfur vacancy formation at the surface, the degradation of I_{DS}^{ON} for holes could also have the same origin, that is, V_S . The mid-gap V_S state on the CB side is localized, while the shallow V_S state on the VB side is easily hybridized with valance band states, which will become more prominent in disulfur vacancies and even sulfur vacancy clusters.^[68] This explains why the sulfur vacancy-induced transport is more prominent on the VB side (conductance peaks in **Figure 5f**) compared to its transport on the CB side (conductance fluctuation in **Figure 4b**). Although Nb_{Mo} could also introduce shallow defect states on the VB

side in *p*-type MoS₂, the density of V_s ($\sim 10^{13}$ cm⁻²)^[31] is much larger than that of Nb_{Mo} ($\sim 10^{12}$ cm⁻²) in atomically thin MoS₂, which indicates that V_s could be the dominant origin of the degraded hole transport. To improve the hole transport at the subthreshold region, continued efforts to improve the crystallinity are required.

3. Conclusion

We successfully extracted the full energy spectra of *D*_{it} from both *n*- and *p*- MoS₂ FETs. By fabricating the 2D heterostructure FET with *h*-BN, on the CB side, it is elucidated that the strain induced externally through the high-*k* deposition process is the dominant origin of the interface degradation which is further enhanced in response to the degree of initial surface roughness. Therefore, the strategy to obtain the sharp switching for *n*-MoS₂ FETs is to develop stress-free high-*k* deposition while maintaining the atomic flatness for the substrate surface. On the other hand, on the VB side, V_s-induced defect states dominate the interface degradation. To improve the hole transport, continued efforts to improve the crystallinity are required.

4. Experimental Section

Device fabrication: *n*-MoS₂ flakes were mechanically exfoliated from natural bulk MoS₂ crystals purchased from SPI Supplies, while *p*-MoS₂ flakes were obtained from Nb-doped bulk MoS₂ crystals purchased from HQ graphene. This Nb doped MoS₂ crystals are grown by chemical vapor transport and have been characterized previously.^[60] For MoS₂/SiO₂ FETs, MoS₂ FETs were directly prepared on SiO₂/Si substrates, while for MoS₂/*h*-BN heterostructure FETs, the details of transfer and stacking processes are shown in **Figure S1** (Supporting Information). Ni/Au were deposited as source/drain electrodes for all FETs. For the high-*k* top-gate formation, 1-nm-thick Y₂O₃ was deposited via thermal evaporation of the Y metal in a PBN crucible in an Ar atmosphere with a partial pressure of 10⁻¹ Pa to form the buffer layer.^[45,46] Al₂O₃ oxide layers with thicknesses of 10 or 30 nm were deposited

via ALD, followed by the Al top-gate electrode formation. No annealing was conducted after the device fabrication. High-*k*/MoS₂ FETs were also fabricated on quartz substrate for suppressing the parasitic capacitance in *C-V* measurements.

Measurements: Raman spectroscopy and AFM were employed to determine the flake crystal quality and thickness. *I-V* and *C-V* measurements were conducted using Keysight B1500 and 4980A LCR meters, respectively. All electrical measurements were performed in a vacuum prober with a cryogenic system.

Supporting Information

Supporting Information is available from the Wiley Online Library or from the author.

Acknowledgements

N. F. was supported by a Grant-in-Aid for JSPS Research Fellows from the JSPS KAKENHI. This research was partly supported by The Canon Foundation, the JSPS Core-to-Core Program, A. Advanced Research Networks, the JSPS A3 Foresight Program, and JSPS KAKENHI Grant Numbers JP16H04343, JP19H00755, and 19K21956, Japan.

References

- [1] S. M. Sze, K. K. Ng, *Physics of Semiconductor Devices*, 3rd ed., John Wiley & Sons, New Jersey, **2007**.
- [2] E. H. Nicollian, J. R. Brews, *MOS Physics and Technology*, Wiley, New York, **1982**.
- [3] F. Heiman, G. Warfield, *IEEE Trans. Electron Devices* **1965**, *12*, 167.
- [4] C. Berglund, *IEEE Trans. Electron Devices* **1966**, *ED-13*, 701.
- [5] Y. Nishi, *Jpn. J. Appl. Phys.* **1971**, *10*, 52.
- [6] E. H. Poindexter, P. J. Caplan, B. E. Deal, R. R. Razouk, *J. Appl. Phys.* **1981**, *52*, 879.
- [7] T. Sakurai, T. Sugano, *J. Appl. Phys.* **1981**, *52*, 2889.
- [8] P. Chow, K. L. Wang, *IEEE Trans. Electron Devices* **1986**, *33*, 1299.
- [9] H. Haddara, M. El-Sayed, *Solid-State Electronics* **1988**, *31*, 1289.
- [10] D. M. Fleetwood, *IEEE Trans. Nuclear Sci.* **1992**, *39*, 269.

- [11] S. Takagi, A. Toriumi, *IEEE Trans. Electron Devices* **1995**, *42*, 2125.
- [12] S. B. Desai, S. R. Madhupathy, A. B. Sachid, J. P. Llinas, Q. Wang, G. H. Ahn, G. Pitner, M. J. Kim, J. Bokor, C. Hu, H. S. P. Wong, A. Javey, *Science* **2016**, *354*, 99.
- [13] H. Liu, D. Y. Peide, *IEEE Electron Device Lett.* **2012**, *33*, 546.
- [14] S. Kim, A. Konar, W. S. Hwang, J. H. Lee, J. Lee, J. Yang, C. Jung, H. Kim, J. B. Yoo, J. Y. Choi, S. Y. Lee, D. Jena, W. Choi, K. Kim, *Nature Commun.* **2012**, *3*, 1011.
- [15] G. A. Salvatore, N. Münzenrieder, C. Barraud, L. Petti, C. Zysset, L. Büthe, K. Ensslin, G. Tröster, *ACS Nano* **2013**, *7*, 8809.
- [16] X. Chen, Z. Wu, S. Xu, L. Wang, R. Huang, Y. Han, W. Ye, W. Xiong, T. Han, G. Long, Y. Wang, Y. He, Y. Cai, P. Sheng, N. Wang, *Nature Commun.* **2015**, *6*, 6088.
- [17] X. Zou, J. Wang, C. H. Chiu, Y. Wu, X. Xiao, C. Jiang, W. We, L. Mai, T. Chen, J. Li, J. C. Ho, L. Liao, *Adv. Mater.* **2014**, *26*, 6255.
- [18] W. Zhu, T. Low, Y. -H. Lee, D. B. Farmer, J. Kong, F. Xia, P. Avouris, *Nature Commun.* **2014**, *5*, 3087.
- [19] N. Ninomiya, T. Mori, N. Uchida, E. Watanabe, D. Tsuya, S. Moriyama, M. Tanaka, A. Ando, *Jpn. J. Appl. Phys.* **2015**, *54*, 046502.
- [20] J. Wang, S. Li, X. Zou, J. Ho, L. Liao, X. Xiao, C. Jiang, W. Hu, J. Wang, J. Li, *Small* **2015**, *11*, 5932.
- [21] K. Choi, S. R. A. Raza, H. S. Lee, P. J. Jeon, A. Pezeshki, S. W. Min, J. S. Kim, W. Yoon, S. Ju, K. Lee, S. Im, *Nanoscale* **2015**, *7*, 5617.
- [22] M. Takenaka, Y. Ozawa, J. Han, S. Takagi, *IEEE International Electron Devices Meeting Tech. Dig.* **2016**, 139.
- [23] S. Park, S. Y. Kim, Y. Choi, M. Kim, H. Shin, J. Kim, W. Choi, *ACS Appl. Mater. Interfaces* **2016**, *8*, 11189.
- [24] P. Zhao, A. Azcatl, Y. Y. Gomeniuk, P. Bolshakov, M. Schmidt, S. J. McDonnell, C. L. Hinkle, P. K. Hurley, R. M. Wallace, C. D. Young, *ACS Appl. Mater. Interfaces* **2017**, *9*, 24348.
- [25] N. Fang, K. Nagashio, *ACS Appl. Mater. interfaces* **2018**, *10*, 32355.
- [26] N. Fang, K. Nagashio, *J. Phys. D* **2018**, *51*, 065110.
- [27] Q. A. Vu, S. Fan, S. H. Lee, M. -K. Joo, W. J. Yu, Y. H. Lee, *2D Mater.* **2018**, *5*, 031001.
- [28] P. Zhao, A. Khosravi, A. Azcatl, P. Bolshakov, G. Mirabelli, E. Caruso, C. Hinkle, P. K. Hurley, R. M. Wallace, C. D. Young, *2D Mater.* **2018**, *5*, 031002.
- [29] K. Taniguchi, N. Fang, K. Nagashio, *Appl. Phys. Lett.* **2018**, *113*, 133505.
- [30] P. Xia, X. Feng, R. J. Ng, S. Wang, D. Chi, C. Li, Z. He, X. L. K.-W. Ang, *Sci. Rep.* **2017**, *7*, 40669.
- [31] J. Hong, Z. Hu, M. Probert, K. Li, D. Lv, X. Yang, J. Zhang, *Nature Commun.* **2015**, *6*, 6293.
- [32] W. Zhou, X. Zou, S. Najmaei, Z. Liu, Y. Shi, J. Kong, J. C. Idrobo, *Nano Lett.* **2013**, *13*, 2615.
- [33] D. Liu, Y. Guo, L. Fang, J. Robertson, *Appl. Phys. Lett.* **2013**, *103*, 183113.
- [34] H. Qiu, T. Xu, Z. Wang, W. Ren, H. Nan, Z. Ni, Q. Chen, S. Yuan, F. Miao, F. Song, G. Long, Y. Shi, L. Sun, J. Wang, X. Wang, *Nature Commun.* **2013**, *4*, 2642.
- [35] S. McDonnell, R. Addou, C. Buie, R. M. Wallace,; C. L. Hinkle, *ACS Nano* **2014**, *8*, 2880.
- [36] P. Vancsó, G. Z. Magda, J. Pető, J. Y. Noh, Y. S. Kim, C. Hwang, L. P. Biró, L. Tapasztó, *Sci. Rep.* **2016**, *6*, 29726.
- [37] S. H. Song, M. -K. Joo, M. Neumann, H. Kim, Y. H. Lee, *Nature Commun.* **2017**, *8*, 2121.
- [38] Y. Y. Illarionov, G. Rzepa, M. Wlatl, T. Knobloch, A. Grill, M. M. Furchi, T. Mueller, T. Grasser, *2D Mater.* **2016**, *3*, 035004.
- [39] B. Shin, G. Han, S. Yun, H. Oh, J. Bae, Y. Song, C. Park, Y. Lee, *Adv. Mater.* **2016**, *28*, 9378.
- [40] Y. Guo, D. Liu, J. Robertson, *Appl. Phys. Lett.* **2015**, *106*, 173106.
- [41] A. V. Kolobov, J. Tominaga, *Two-Dimensional Transition-Metal Dichalcogenides*, Springer Series in Materials Science 239, Springer, Switzerland, **2016**.
- [42] N. Ma, D. Jena, *2D Mater.* **2015**, *2*, 015003.
- [43] S. Toyoda, T. Uwanno, T. Taniguchi, K. Watanabe, K. Nagashio, *Appl. Phys. Express* **2019**, *12*, 055008.
- [44] T. Uwanno, Y. Hattori, T. Taniguchi, K. Watanabe, K. Nagashio, *2D Mater.* **2015**, *2*, 041002.
- [45] N. Takahashi, K. Nagashio, *Appl. Phys. Express* **2016**, *9*, 125101.
- [46] S. Kurabayashi, K. Nagashio, *Nanoscale* **2017**, *9*, 13264.
- [47] K. Uchida, J. Koga, R. Ohba, T. Numata, S. I. Takagi, *IEEE International Electron Devices Meeting Tech. Dig.* **2001**, 633.
- [48] A. Kuc, N. Zibouche, T. Heine, *Phys. Rev. B* **2011**, *83*, 245213.
- [49] J. K. Ellis, M. J. Lucero, G. E. Scuseria, *Appl. Phys. Lett.* **2011**, *99*, 261908.
- [50] S. Ghatak, A. N. Pal, A. Ghosh, *ACS Nano* **2011**, *5*, 7707.
- [51] D. Jariwala, V. K. Sangwan, D. J. Late, J. E. Johns, V. P. Dravid, T. J. Marks, L. J. Lauhon, M. C. Hersam, *Appl. Phys. Lett.* **2013**, *102*, 173107.
- [52] B. R. Matis, N. Y. Garces, E. R. Cleveland, B. H. Houston, J. W. Baldwin, *ACS Appl. Mater. Interfaces* **2017**, *9*, 27995.
- [53] N. Fang, K. Nagashio, A. Toriumi, *Appl. Phys. Express* **2015**, *8*, 065203.
- [54] N. Fang, K. Nagashio, A. Toriumi, *2D Mater.* **2016**, *4*, 015035.

- [55] Y. J. Zhang, J. T. Ye, Y. Yomogida, T. Takenobu, Y. Iwasa, *Nano Lett.* **2013**, *13*, 3023.
- [56] W. Bao, X. Cai, D. Kim, K. Sridhara, M. S. Fuhrer, *Appl. Phys. Lett.* **2013**, *102*, 042104.
- [57] S. Chuang, C. Battaglia, A. Azcatl, S. McDonnell, J. S. Kang, X. Yin, M. Tosun, R. Kapadia, H. Fang, R. M. Mallace, A. Javey, *Nano Lett.* **2014**, *14*, 1337.
- [58] Y. Liu, J. Guo, E. Zhu, L. Liao, S. -J. Lee, M. Ding, I. Shakir, V. Gambin, Y. Huang, X. Duan, *Nature* **2018**, *557*, 696.
- [59] K. Dolui, I. Rungger, C. D. Pemmaraju, S. Sanvito, *Phys. Rev. B* **2013**, *88*, 075420.
- [60] J. Suh, T. E. Park, D. Y. Lin, D. Fu, J. Park, H. J. Jung, Y. Chen, C. Ko, C. Jang, Y. Sun, R. Sinclair, J. Chang, S. Tongay, J. Wu, *Nano Lett.* **2014**, *14*, 6976.
- [61] C. Lee, H. Yan, L. E. Brus, J. Hone, S. Ryu, *ACS Nano* **2010**, *4*, 2695.
- [62] H. Li, Q. Zhang, C. C. R. Yap, B. K. Tay, T. H. T. Edwin, A. Olivier, D. Baillargeat, *Adv. Funct. Mater.* **2012**, *22*, 1385.
- [63] R. Moriya, T. Yamaguchi, Y. Inoue, Y. Sata, S. Morikawa, S. Masubuchi, T. Machida, *Appl. Phys. Lett.* **2015**, *106*, 223103.
- [64] M. D. Siao, W. C. Shen, R. S. Chen, Z. W. Chang, M. C. Shih, Y. P. Chiu, C. M. Cheng, *Nature Commun.*, **2018**, *9*, 1442.
- [65] S. Das, H. Chen, A. Penumatcha, J. Appenzeller, *Nano Lett.* **2012**, *13*, 100-105.
- [66] A. Penumatcha, R. Salazar, J. Appenzeller, *Nat. Commun.* **2015**, *6*, 8948.
- [67] E. Ponomarev, A. Pasztor, A. Waelchli, A. Scarfato, N. Ubrig, C. Renner, A. F. Morpurgo, *ACS Nano* **2018**, *12*, 2669.
- [68] Y. -C. Lin, T. Bjokman, H. -P. Komsa, P. -Y. Teng, C. -H. Yeh, F. -S. Huang, K. -H. Lin, J. Jadcak, Y. -S. Huang, P. -W. Chiu, A. V. Krasheninnikov, *Nature Commun.* **2015**, *6*, 6736.

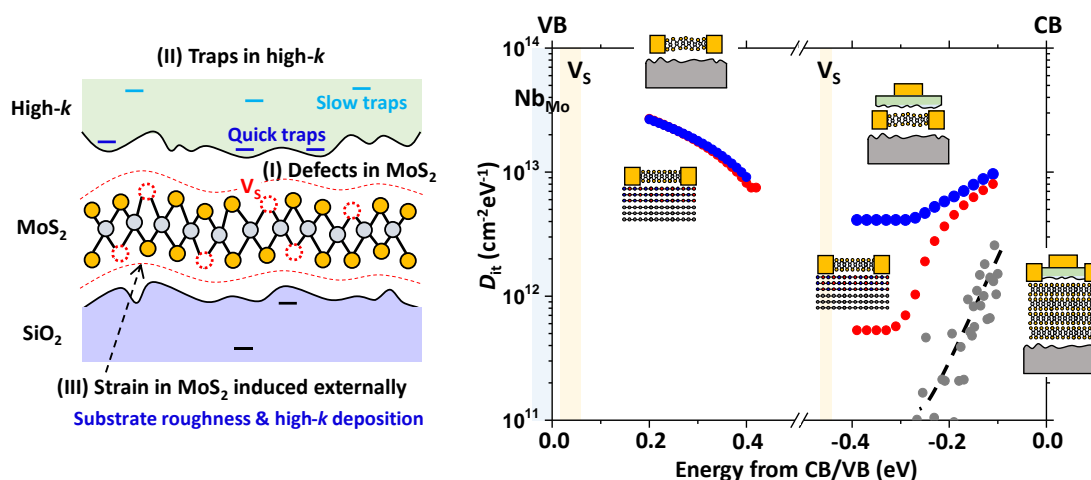
The table of contents entry

The interfacial properties of both *n*- and *p*- MoS₂ FETs with a wide thickness range and various gate stack structures are investigated. Full energy spectra of the interface state densities are extracted. The external strain dominates the interface at the conduction band side, while sulfur-vacancy-induced defect-states dominate the valance band side.

Keyword: two-dimensional material, heterostructure, defect states, quantum capacitance

N. Fang, S. Toyoda, T. Taniguchi, K. Watanabe, K. Nagashio

Full energy spectra of interface state densities for *n*- and *p*-type MoS₂ field-effect transistors



Supporting Information

Full energy spectra of interface state densities for *n*- and *p*-type MoS₂ field-effect transistors

Nan Fang, Satoshi Toyoda, Takashi Taniguchi, Kenji Watanabe, and Kosuke Nagashio*

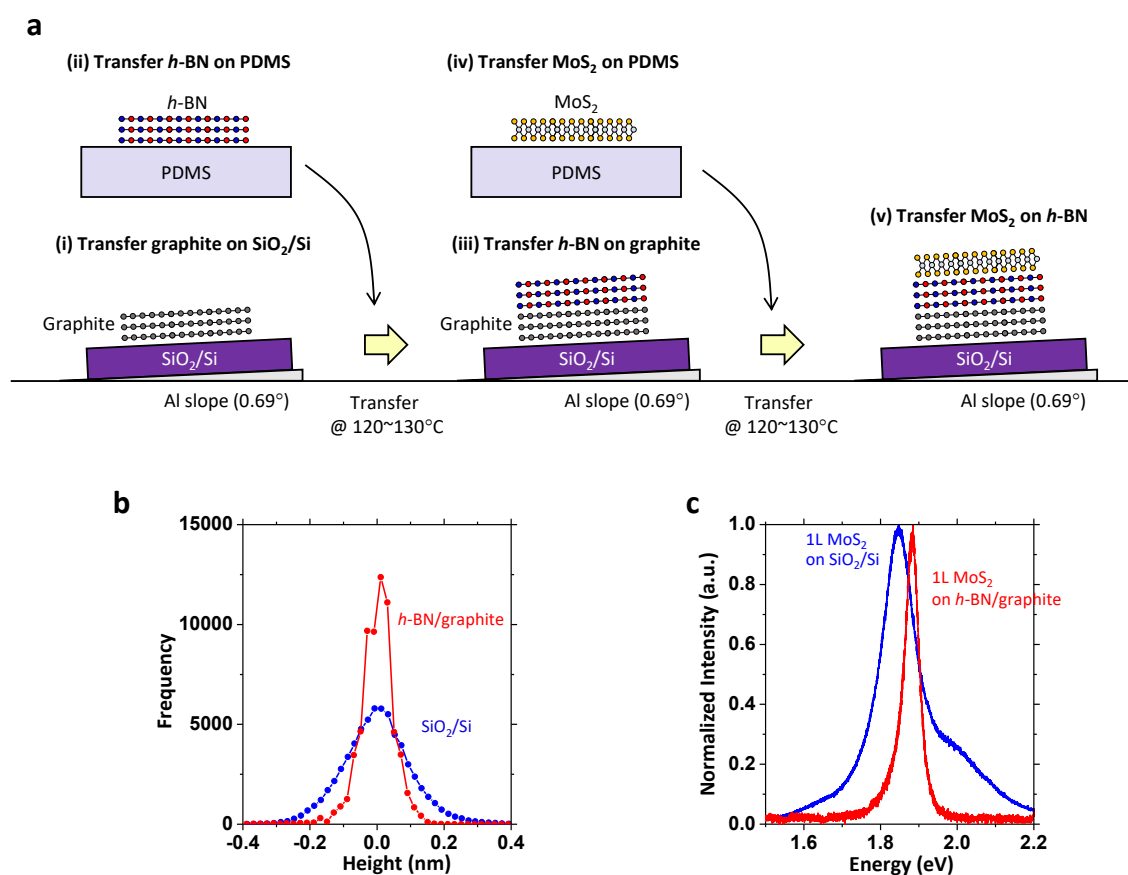


Figure S1. (a) Schematics of the fabrication process for MoS₂/*h*-BN/graphite heterostructure. Graphite flakes are first prepared on SiO₂/Si substrate by mechanical exfoliation. *h*-BN flakes are prepared on PDMS by mechanical exfoliation, and then transferred on graphite by using the micromanipulator system with slope of ~ 0.69° at 120 ~ 130°C. MoS₂ flakes are prepared on PDMS by mechanical exfoliation, and again transferred on *h*-BN/graphite to form MoS₂/*h*-BN/graphite heterostructure. (b) Height histogram of *h*-BN/graphite and SiO₂/Si, respectively. (c) Photoluminescence (PL) of 1L MoS₂ on SiO₂/Si and *h*-BN/graphite, respectively. Compared with PL peak on SiO₂/Si substrate, it is sharper on *h*-BN/graphite, which might be attributed to the reduced surface roughness and doping effect.

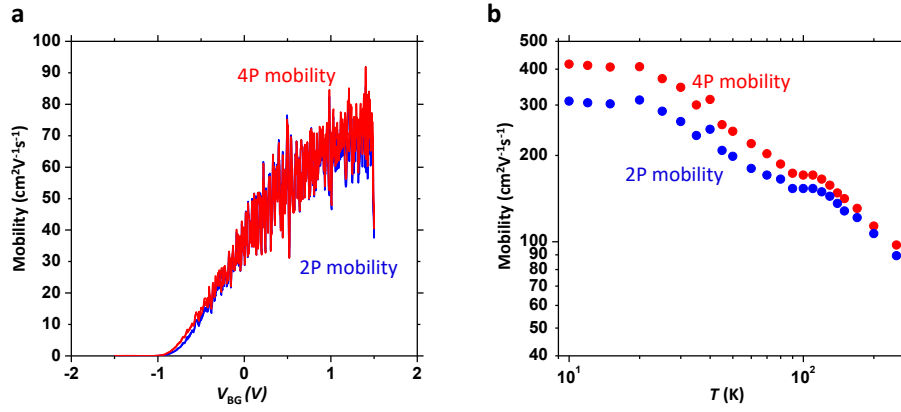


Figure S2. (a) 2P and 4P field-effect mobility as a function of V_{BG} for the $\text{MoS}_2/h\text{-BN/graphite}$ heterostructure FET. 2P and 4P mobility are comparable with each other, which indicates the ohmic contact by Ni. (b) 2P and 4P field-effect mobility as a function of temperature. A clear phonon-limited temperature dependence is observed, which indicates the high interface properties of the $\text{MoS}_2/h\text{-BN/graphite}$ heterostructure.

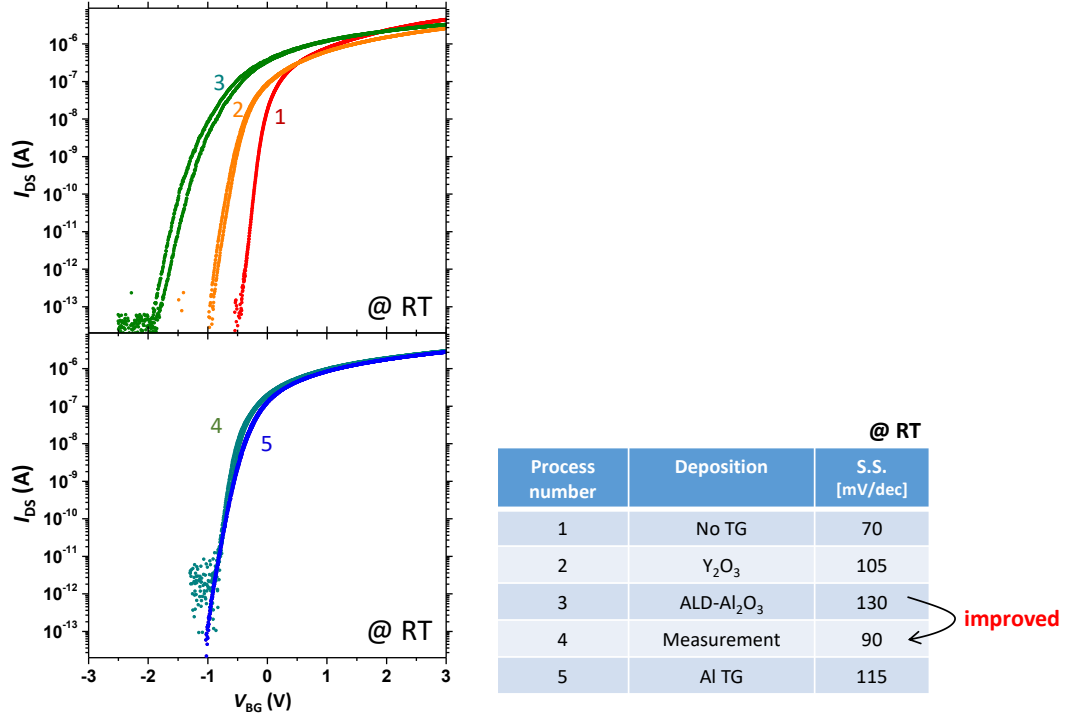


Figure S3. I_{DS} - V_{BG} characteristics of 1L MoS₂/h-BN/graphite heterostructure FET at $V_{DS} = 0.1$ V and RT. The number in the figures indicates the process number in the table. 1: before top-gate deposition, 2: after Y buffer layer deposition, 3: after ALD-Al₂O₃ deposition, 4: the 2nd electrical measurement, 5: after Al deposition for the top-gate electrode. The sample was always kept in the vacuum desiccator to avoid unintentional doping and so on from the lab environment if the device was not measured just after the top gate fabrication processes.

Interestingly, $S.S.$ was unintentionally recovered to ~ 90 mVdec⁻¹ from 130 mVdec⁻¹ when this device was measured again after a few days' storage in the vacuum desiccator and before the Al top-gate deposition (step 4). This strongly indicates that the degradation of both D_{it} and hysteresis originates mainly from the strain induced by high- k deposition process, and the strain was released at step 4. Since the maximum temperature during the measurement is RT, the strain might be released by the thermal energy of ~ 25 meV, which is close to E_h in Figure 4e. Noted that similar improvement of $S.S.$ was encountered for other samples.

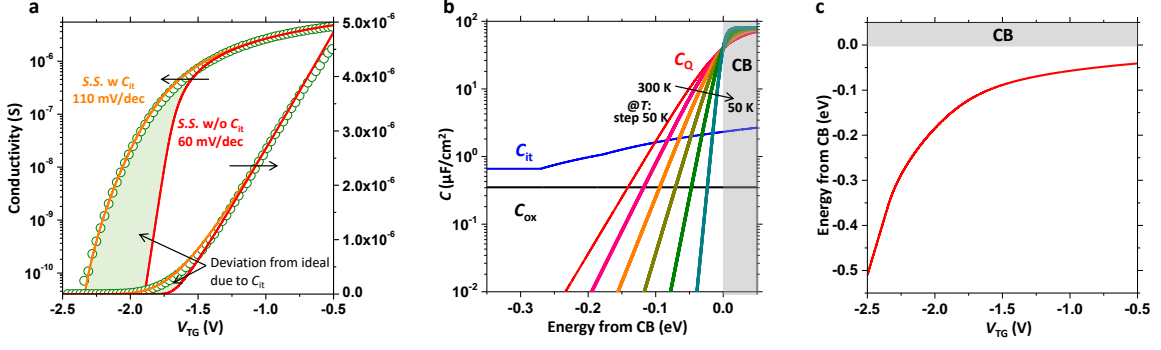


Figure S4. (a) $I_{DS}-V_{TG}$ characteristics of a high- $k/1L$ MoS₂/SiO₂ FET at $V_{DS} = 0.1$ V and RT, and the modelling results. (b) The energy distribution of C_Q , C_{ox} and C_{it} used in the modelling. (c) E_F-V_{TG} relation extracted by the modelling.

Modelling: In this model, the electron transport process is considered through the Drude model.^[1,2] Conductivity $\sigma = en_{ch}\mu_d$, where n_{ch} and μ_d refer to channel carrier density and drift mobility, respectively. μ_d is experimentally extracted as constant field-effect mobility at strong linear region of the $I-V$ curve. MoS₂ channel carrier density is estimated through oxide capacitance (C_{ox}), quantum capacitance (C_Q), and interface states capacitance (C_{it}). C_{ox} is determined experimentally, while C_Q is theoretically calculated at different temperature using the following relation^[1] $C_Q = e^2 g_{2D} \left[1 + \frac{\exp(E_G / 2k_B T)}{2 \cosh(E_F / k_B T)} \right]$, where $g_{2D} = g_s g_v m^* / 2\pi\hbar^2$ is the band-

edge DOS, and E_G is the bandgap. Here, bandgap $E_G = 1.9$ eV for monolayer MoS₂. g_s and g_v are the spin and valley degeneracy factors, respectively. m^* is assumed to be $0.6m_0$. The mid gap is defined to be $E_F = 0$ eV. The energy distribution of C_{ox} and C_Q can be seen in (b). When the ideal $I_{DS}-V_{TG}$ curve is calculated using C_{ox} and C_Q with constant μ value extracted experimentally, ideal S.S. of 60 mV/dec can be obtained, as shown by solid red line in (a). The deviation between ideal and experimental $I_{DS}-V_{TG}$ (hatched region in (a)) can be considered as the contribution of electron traps to the interface states, that is, C_{it} . Therefore, C_{it} is used as a fitting parameter to reproduce the $I_{DS}-V_{TG}$ curve, as shown by solid orange line in (a). Finally, the energy distribution of D_{it} can be obtained from C_{it} through $C_{it} = e^2 D_{it}$.

It should be noted that extracted D_{it} is still valid even under the constant mobility assumption. The carrier dependent mobility at 300 K has already been calculated in the ref. [1]. Although the mobility increases by more than one order with increasing n_{ch} from 10^{12} to 10^{13} cm⁻², it is ‘‘almost constant’’ at the range of 10^{10} - 10^{11} cm⁻² (subthreshold region). Therefore, present assumption is still valid. Of course, the mobility value itself is much lower than that at the linear region. But, simply say, as can be understood by the fact that D_{it} can be extracted from the S.S. value (i.e., the slope of I_d-V_g), the absolute value of I_d (the mobility value itself) is not important. However, the carrier dependent mobility needs to be considered at linear region.

Threshold voltage (V_{th}) shift: The nature of C_Q explains many temperature dependent electrical properties of atomically thin MoS₂ FET. For example, V_{th} always shift positively with lowering the temperature because C_Q gets close to conduction band (CB). Moreover, this C_Q induced V_{th} shift will be amplified by C_{it} , which attributes to the larger threshold voltage shift in Figure 4b compared with that in Figure 4a in the main text.

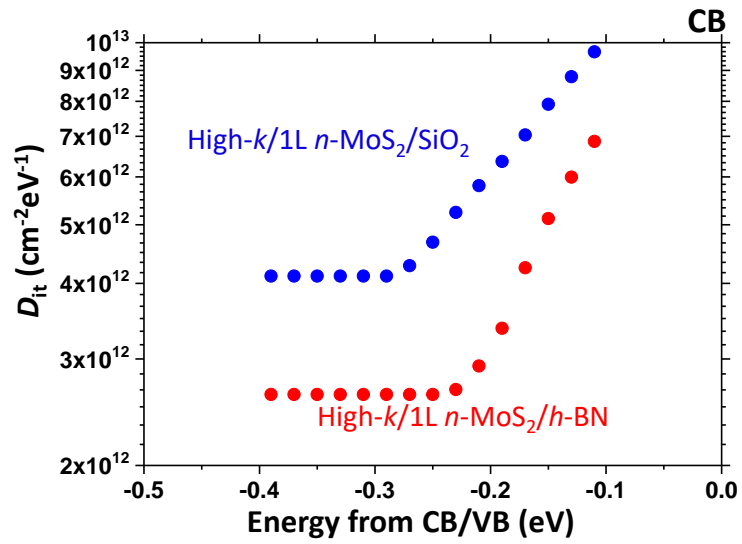


Figure S5. The energy spectra of D_{it} for high- k /1L n -MoS₂/SiO₂ and high- k /1L n -MoS₂/h-BN FETs obtained from top-gate voltage sweep.

References

- [1] N. Ma, D. Jena, *2D Mater.* **2015**, *2*, 015003.
- [2] N. Fang, K. Nagashio, *J. Phys. D* **2018**, *51*, 065110.